

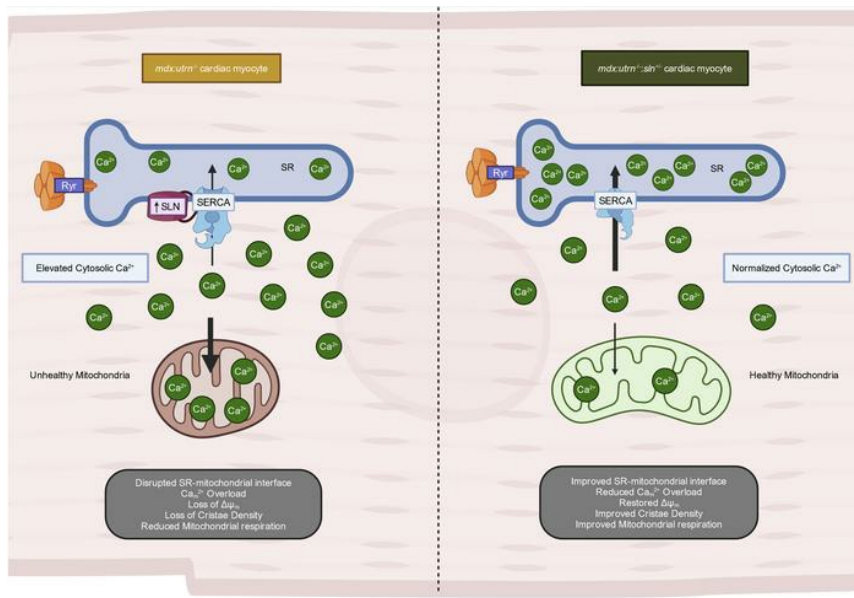
## Improved mitochondrial function in the heart of sarcolipin-deficient dystrophin and utrophin double knockout mice

Satvik Mareedu, ... , Lai-Hua Xie, Gopal J. Babu

JCI Insight. 2024. <https://doi.org/10.1172/jci.insight.170185>.

Research In-Press Preview Metabolism

### Graphical abstract



Find the latest version:

<https://jci.me/170185/pdf>



**Improved mitochondrial function in the heart of sarcolipin-deficient dystrophin and utrophin double knockout mice**

Satvik Mareedu<sup>1</sup>, Nadezhda Fefelova<sup>1</sup>, Cristi L. Galindo<sup>2</sup>, Goutham Prakash<sup>1</sup>, Risa Mukai<sup>1</sup>,  
Junichi Sadoshima<sup>1</sup>, Lai-Hua Xie<sup>1</sup>, Gopal J Babu<sup>1\*</sup>

<sup>1</sup>Department of Cell Biology and Molecular Medicine, New Jersey Medical School, Rutgers University, Newark, NJ 07103, <sup>2</sup>Vascular Medicine Institute & Cardiology, University of Pittsburgh, Pittsburgh, PA 15213.

\*Corresponding author

Gopal J Babu, PhD

Department of Cell Biology and Molecular Medicine

Rutgers, New Jersey Medical School

185 South Orange Ave, Newark, NJ 07103

p. 973-972-5376 f. 973-972-7489

Email: [babugo@njms.rutgers.edu](mailto:babugo@njms.rutgers.edu)

**Conflict-of-interest:** The authors have declared that no conflict of interest exists.

## ABSTRACT

Duchenne muscular dystrophy (DMD) is a progressive muscle-wasting disease associated with cardiomyopathy. DMD-cardiomyopathy is characterized by abnormal intracellular  $\text{Ca}^{2+}$  homeostasis and mitochondrial dysfunction. We used dystrophin and utrophin null (*mdx:utr<sup>n/-</sup>*) mice in sarcolipin (SLN) heterozygous knockout (*sln<sup>+/-</sup>*) background to examine the effect of SLN reduction on mitochondrial function in the dystrophic myocardium. Germline reduction of SLN expression in *mdx:utr<sup>n/-</sup>* mice improved cardiac sarco/endoplasmic reticulum (SR)  $\text{Ca}^{2+}$  cycling, reduced cardiac fibrosis, and improved cardiac function. At the cellular level, reducing SLN expression prevented mitochondrial  $\text{Ca}^{2+}$  overload, reduced mitochondrial membrane potential loss, and improved mitochondrial function. Transmission electron microscopy of myocardial tissues and proteomic analysis of mitochondria-associated membranes show that reducing SLN expression improved mitochondrial structure and SR-mitochondria interactions in dystrophic cardiac myocytes. These findings indicate that SLN upregulation plays a significant role in the pathogenesis of cardiomyopathy and that reducing SLN expression has clinical implications in the treatment of DMD-cardiomyopathy.

## INTRODUCTION

Duchenne muscular dystrophy (DMD) is an X-linked disorder caused by mutations in the dystrophin gene. Lack of dystrophin, being the prime cause of the disease, displays clinical manifestations, such as continuous reduction in muscle function, making the children bedridden by the start of the second decade. As age progresses, DMD patients start to manifest altered cardiac parameters and respiratory weakness (1, 2). While progressive respiratory failure remains the most common cause of death, increased life expectancy has revealed the importance of cardiomyopathy, which accounts for ~ 40% of deaths in the DMD population (3). In this context, it is important to understand the underlying molecular mechanisms causing dystrophic cardiomyopathy and heart failure to identify novel therapeutic targets.

In DMD, abnormal  $\text{Ca}^{2+}_i$  homeostasis is considered one of the major secondary changes that cause muscle pathology and cardiomyopathy (4). The absence of dystrophin protein destabilizes the membrane integrity resulting in stress-induced membrane tears and is associated with calcium ( $\text{Ca}^{2+}$ ) leak leading to abnormal elevation of intracellular  $\text{Ca}^{2+}$  ( $\text{Ca}^{2+}_i$ ) concentration, upregulation of inflammatory factors, and mitochondrial dysfunction, ultimately leading to muscle degeneration, necrosis, and cardiomyopathy(4-8). In addition to the activation of various sarcolemmal  $\text{Ca}^{2+}$  channels, defects in sarco/endoplasmic reticulum (SR)  $\text{Ca}^{2+}$  handling are shown to contribute to the chronic elevation of  $\text{Ca}^{2+}_i$  concentration (4). Under normal physiological conditions, increased cytoplasmic  $\text{Ca}^{2+}$  levels have been shown to increase mitochondrial  $\text{Ca}^{2+}$  ( $\text{Ca}^{2+}_m$ ) uptake, resulting in increased metabolism (9). On the other hand, during pathological conditions, abnormal elevation of  $\text{Ca}^{2+}_m$  content can result in the opening of the mitochondrial permeability transition pore (mPTP), causing mitochondrial dysfunction and cell death (10, 11). It has been shown that in dystrophic hearts,  $\text{Ca}^{2+}_m$  levels are elevated and associated with defective

mitophagy (12, 13). During cardiac pathology, SR-mediated cytoplasmic  $\text{Ca}^{2+}$  rise caused by increased SR  $\text{Ca}^{2+}$  leak via ryanodine receptor (RyR), along with decreased SR  $\text{Ca}^{2+}$  uptake via sarco/endoplasmic reticulum  $\text{Ca}^{2+}$  ATPase (SERCA), can increase  $\text{Ca}^{2+}_m$  concentration, indicating that there is a close association between SR and mitochondria (14, 15). Therefore, it is important to determine whether improving SR  $\text{Ca}^{2+}$  handling can improve  $\text{Ca}^{2+}_m$  handling and mitochondrial function in dystrophic heart.

We recently demonstrated that the expression of sarcolipin (SLN), a potent inhibitor of the SERCA pump, is increased in dystrophic muscles and the heart of animal models and human DMD (16, 17). Furthermore, in mouse models of DMD, reducing SLN expression is sufficient to improve SR  $\text{Ca}^{2+}$  handling and mitigate DMD and associated cardiomyopathy (17, 18). Our studies also demonstrated that reducing SLN expression can improve mitochondrial-mediated energy metabolism in *mdx* muscles (19). However, the causal link between SLN upregulation, SR  $\text{Ca}^{2+}$  handling, and  $\text{Ca}^{2+}_m$  load and its effect on mitochondrial function in dystrophic myocardium has not been studied. Therefore, the major goal of this study was to establish whether SLN upregulation is linked to mitochondrial dysfunction in dystrophic myocardium. Here, using dystrophin and utrophin deficient (*mdx:utrn*<sup>-/-</sup>) mice as a model system, we tested the hypothesis that reducing SLN expression is sufficient to improve cardiac SERCA function, SR  $\text{Ca}^{2+}$  cycling, and thereby  $\text{Ca}^{2+}_m$  content, and mitochondrial function in dystrophic myocardium.

## RESULTS

### Reducing SLN expression improved SR Ca<sup>2+</sup> handling and cardiac contractility in *mdx:utrn*<sup>-/-</sup> mice.

We previously demonstrated that ablating one SLN allele (*sln*<sup>+/-</sup>) is sufficient to normalize SLN expression, mitigate severe muscular dystrophy, and improve cardiac function in *mdx:utrn*<sup>-/-</sup> mice (17). Therefore, to test our hypothesis, we chose *mdx:utrn*<sup>-/-</sup>:*sln*<sup>+/-</sup> mice.

We first measured cardiac function using M-mode echocardiography. Results show that the systolic function of the heart as measured by the left ventricular (LV) ejection fraction (EF) and fractional shortening (FS) were significantly improved in *mdx:utrn*<sup>-/-</sup>:*sln*<sup>+/-</sup> mice compared to that of age-and sex-matched *mdx:utrn*<sup>-/-</sup> mice (**Supplementary Table 1**). Pulse wave Doppler analysis shows that the ratio between early (E) and late (atrial-A) ventricular filling velocity (E/A) was significantly reduced, and the myocardial performance index (MPI) was significantly increased in *mdx:utrn*<sup>-/-</sup> mice compared to that of WT controls. On the other hand, the E/A ratio was significantly increased, and MPI was decreased in *mdx:utrn*<sup>-/-</sup>:*sln*<sup>+/-</sup> mice (**Supplementary Figure 1**). Histopathological examination of ventricular sections using Picrosirius red (PSR) staining shows that *mdx:utrn*<sup>-/-</sup> mice developed severe cardiac fibrosis as evidenced by increased collagen accumulation. On the other hand, collagen accumulation was significantly reduced in the ventricles of *mdx:utrn*<sup>-/-</sup>:*sln*<sup>+/-</sup> mice (**Supplementary Figure 2**). These findings together indicate that reducing SLN expression attenuated cardiac fibrosis, prevented diastolic dysfunction, and improved the overall cardiac function in *mdx:utrn*<sup>-/-</sup> mice.

We next examined the Ca<sup>2+</sup> handling properties of cardiac myocytes from WT, *mdx:utrn*<sup>-/-</sup> and *mdx:utrn*<sup>-/-</sup>:*sln*<sup>+/-</sup> mice. The results show significantly higher amplitudes of twitch-Ca<sup>2+</sup> transients (**Figure 1A**), increased SR Ca<sup>2+</sup> content represented by increased caffeine-induced

Ca<sup>2+</sup> transients amplitudes (**Figure 1B**), decreased SR Ca<sup>2+</sup> uptake represented by the increased time taken for the 50% decrease in twitch Ca<sup>2+</sup> transients ( $T_{50}$ ; **Figure 1C**), decreased Ca<sup>2+</sup> removal from the cytoplasm represented by increased  $T_{50}$  of caffeine-induced Ca<sup>2+</sup> transients (**Figure 1D**) and defective RyR function represented by increased fractional Ca<sup>2+</sup> release (**Figure 1E**) in myocytes from *mdx:utrn*<sup>-/-</sup> mice. On the other hand, in myocytes from *mdx:utrn*<sup>-/-</sup>:*sln*<sup>+/-</sup> mice, all of these parameters except for the caffeine-induced Ca<sup>2+</sup> transients were restored to levels comparable to WT myocytes (**Figures 1A-1E**).

Western blot analyses show that the SLN protein level, which was significantly higher in the ventricles of *mdx:utrn*<sup>-/-</sup> mice, was reduced in the ventricles of *mdx:utrn*<sup>-/-</sup>:*sln*<sup>+/-</sup> mice and was similar to that of WT control ventricles. The protein levels of SERCA2a, phospholamban (PLN), RyR2, and calcineurin were unaltered and comparable in the ventricles of WT, *mdx:utrn*<sup>-/-</sup> and *mdx:utrn*<sup>-/-</sup>:*sln*<sup>+/-</sup> mice (**Supplementary Figure 3**).

### **Reducing SLN expression prevents mitochondrial Ca<sup>2+</sup> overload and improves mitochondrial function in the *mdx:utrn*<sup>-/-</sup> myocardium.**

We next examined whether improving the SR Ca<sup>2+</sup> handling via reducing SLN expression improves Ca<sup>2+</sup><sub>m</sub> cycling in dystrophic cardiac myocytes. Rhod-2, AM, a high-affinity Ca<sup>2+</sup> indicator that selectively localizes to mitochondria, was used to determine the Ca<sup>2+</sup><sub>m</sub> content in cardiac myocytes using confocal imaging. The mean fluorescence intensity (MFI) of Rhod-2 was significantly higher in *mdx:utrn*<sup>-/-</sup> ventricular myocytes (**Figure 2A**) indicating increased Ca<sup>2+</sup><sub>m</sub> content. The MFI in *mdx:utrn*<sup>-/-</sup>:*sln*<sup>+/-</sup> ventricular myocytes, on the other hand, was significantly lower and comparable to that of WT controls (**Figure 2A**).

To further validate our findings, we examined  $\text{Ca}^{2+}_m$  efflux, an indirect measurement of  $\text{Ca}^{2+}_m$  content as described before (12, 20). In brief, plasmalemmal  $\text{Ca}^{2+}$  influx was first blocked by treating myocytes with  $\text{Li}^+$  Tyrode's solution devoid of  $\text{Na}^+$  and  $\text{Ca}^{2+}$ , followed by tetracaine and thapsigargin treatment, which inhibits SR  $\text{Ca}^{2+}$  release and uptake, respectively. Myocytes were then treated with FCCP and oligomycin to release  $\text{Ca}^{2+}$  from mitochondria, resulting in an increase in cytosolic  $\text{Ca}^{2+}$  levels (referred to as  $\text{Ca}^{2+}_m$  efflux or transients), which serves as an indirect measure of  $\text{Ca}^{2+}_m$  content (**Supplementary Figure 4**).  $\text{Ca}^{2+}_m$  efflux was significantly higher in myocytes from *mdx:utr<sup>-/-</sup>* mice, whereas it was significantly lower in myocytes from *mdx:utr<sup>-/-</sup>:sln<sup>+/-</sup>* mice and comparable to WT controls (**Figure 2B**). These results indicate that  $\text{Ca}^{2+}_m$  content was higher in myocytes from *mdx:utr<sup>-/-</sup>* mice, whereas reducing SLN expression prevents  $\text{Ca}^{2+}_m$  overload in *mdx:utr<sup>-/-</sup>* myocytes.

Western blot analyses show that the protein level of the leucine zipper and EF-hand containing transmembrane protein 1 (LETM1), mitochondrial  $\text{Na}^{2+}/\text{Ca}^{2+}$  exchanger (NCLX), and canonical transient receptor potential 1 (TRPC1) were not different between the hearts of all three groups of mice (**Supplementary Figure 5**). On the other hand, mitochondrial  $\text{Ca}^{2+}$  uniporter (MCU) was significantly higher in the ventricles of both *mdx:utr<sup>-/-</sup>* and *mdx:utr<sup>-/-</sup>:sln<sup>+/-</sup>* mice compared to that of WT controls (**Figure 2C**). MICU1, an MCU subunit that regulates channel opening, was significantly lower in the *mdx:utr<sup>-/-</sup>* ventricles than in the WT and *mdx:utr<sup>-/-</sup>:sln<sup>+/-</sup>* ventricles (**Figure 2C**).

$\text{Ca}^{2+}_m$  levels are known to regulate mitochondrial respiration. Therefore, we next examined the expression levels and activities of various electron complex chain subunits. Western blot analyses show that the protein levels of Complexes I (NDUF88), II (SDHB), III (UQCRC2), IV (MTCO1), or V (ATP5A) subunits in the ventricles of WT, *mdx:utr<sup>-/-</sup>* and *mdx:utr<sup>-/-</sup>:sln<sup>+/-</sup>* mice



were not significantly different (**Figures 3A**). Complex I and complex IV activity in ventricular lysates from WT, *mdx:utrn*<sup>-/-</sup>, and *mdx:utrn*<sup>-/-</sup>:*sln*<sup>+/-</sup> mice were comparable and not significantly different (**Figure 3B**).

Complex II dysfunction has been reported in many neurodegenerative diseases and aging (21). We, therefore, examined complex II respiration in intact mitochondria prepared from fresh ventricular tissues using the Seahorse XFe24 flux analyzer. Complex II-driven respiration was significantly lower in *mdx:utrn*<sup>-/-</sup> ventricular mitochondria compared to that of WT controls. On the other hand, complex II-driven respiration was significantly improved in *mdx:utrn*<sup>-/-</sup>:*sln*<sup>+/-</sup> ventricular mitochondria and comparable to WT controls (**Figures 3C**). The maximal rates of state III (ADP stimulated) and state III<sub>μ</sub> (FCCP stimulated) respiration were significantly reduced in *mdx:utrn*<sup>-/-</sup> ventricular mitochondria. However, the lower state III<sub>μ</sub> respiration indicates that the FCCP concentration may have had an inhibitory effect on the respiratory function in these experiments. Despite this effect, state III and III<sub>μ</sub> respirations were significantly higher and comparable to WT controls in *mdx:utrn*<sup>-/-</sup>:*sln*<sup>+/-</sup> ventricular mitochondria (**Figure 3D**). The respiratory control ratio (RCR), which represents mitochondrial health, was significantly lower in *mdx:utrn*<sup>-/-</sup> ventricles compared to WT controls. Although not statistically significant, RCR was higher in the mitochondria of *mdx:utrn*<sup>-/-</sup>:*sln*<sup>+/-</sup> ventricles (**Figure 3E**).

### **Reducing SLN expression prevents mitochondrial membrane potential loss in dystrophic ventricular myocytes.**

Mitochondrial dysfunction is normally associated with either loss of membrane potential or elevated oxidative stress. We first assessed mitochondrial membrane potential ( $\Delta\Psi_m$ ) in isolated cardiac myocytes using the ratiometric dye JC-1, as well as MitoTracker Red CMXRos

that accumulates in mitochondria in live cells depending upon membrane potential (22). The mean red/green fluorescence intensity ratio of JC-1 in myocytes from *mdx:utrn*<sup>-/-</sup> mice was significantly lower indicating mitochondrial depolarization, whereas it was significantly higher in the *mdx:utrn*<sup>-/-</sup>:*sln*<sup>+/-</sup> myocytes (**Figures 4A & 4B**). Similarly, the MFI of MitoTracker Red CMXRos in myocytes from *mdx:utrn*<sup>-/-</sup> mice was significantly lower, whereas the MFI was higher in *mdx:utrn*<sup>-/-</sup>:*sln*<sup>+/-</sup> myocytes and comparable to that of WT myocytes (**Figures 4A & 4C**). These data indicate that there is a loss of  $\Delta\Psi_m$  in myocytes from *mdx:utrn*<sup>-/-</sup> mice and reducing SLN expression prevents  $\Delta\Psi_m$  loss.

We next examined whether oxidative stress contributes to the  $\Delta\Psi_m$  loss in myocytes from *mdx:utrn*<sup>-/-</sup> mice by measuring protein carbonylation and lipid peroxidation using OxyBlot and 4-Hydroxynonenal (4-HNE) staining, respectively. The protein carbonylation and lipid peroxidation in total protein extract (**Figure 4D**) as well as in the purified mitochondrial fractions (**Supplementary Figure 6**) were similar between WT, *mdx:utrn*<sup>-/-</sup>, and *mdx:utrn*<sup>-/-</sup>:*sln*<sup>+/-</sup> ventricles. The protein level of manganese-dependent superoxide dismutase 2 (MnSOD/SOD2), a major mitochondrial anti-oxidant enzyme, was also similar between WT, *mdx:utrn*<sup>-/-</sup> and *mdx:utrn*<sup>-/-</sup>:*sln*<sup>+/-</sup> ventricles. (**Figure 4E**).

### **Reducing SLN expression restores mitochondrial morphology in dystrophic myocardium.**

We then measured mitochondrial number, surface area, and aspect ratio in ventricular sections using transmission electron microscopy (TEM) to determine whether reducing  $Ca^{2+}_m$  load affected mitochondrial morphology in *mdx:utrn*<sup>-/-</sup>:*sln*<sup>+/-</sup> myocardium (**Figure 5A**). The number of mitochondria in *mdx:utrn*<sup>-/-</sup> ventricles was significantly higher than in WT and *mdx:utrn*<sup>-/-</sup>:*sln*<sup>+/-</sup> ventricles (**Figure 5B**). Furthermore, mitochondria from *mdx:utrn*<sup>-/-</sup> ventricles have a smaller

surface area (**Figure 5C**) and aspect ratio (**Figure 5D**). The mitochondrial surface area and aspect ratio in the *mdx:utrn<sup>-/-</sup>:sln<sup>+/-</sup>* ventricles, on the other hand, were significantly higher and comparable to WT ventricles (**Figures 5C & 5D**). The mitochondrial copy number assessed by quantitative PCR (qPCR), however, was significantly low in the ventricles of both *mdx:utrn<sup>-/-</sup>* and *mdx:utrn<sup>-/-</sup>:sln<sup>+/-</sup>* mice (**Figure 5E**).

### **Reducing SLN expression improves both SR and non-SR-associated mitochondrial structure in dystrophic myocardium.**

We next examined the mitochondrial structure, particularly cristae density, in the ventricles of WT, *mdx:utrn<sup>-/-</sup>* and *mdx:utrn<sup>-/-</sup>:sln<sup>+/-</sup>* mice using TEM (**Figure 6A**). Quantitation shows that there was a significant reduction in cristae density in the mitochondria from *mdx:utrn<sup>-/-</sup>* ventricles. These reductions in cristae density were more pronounced in SR-associated mitochondria than in non-SR-associated mitochondria. The cristae density was significantly higher in both SR-associated and non-SR-associated mitochondria from *mdx:utrn<sup>-/-</sup>:sln<sup>+/-</sup>* ventricles than in *mdx:utrn<sup>-/-</sup>* ventricles (**Figure 6A**).

We next examined the SR-mitochondrial junctions by analyzing the mitochondria-associated membranes (MAMs). The purity of the MAMs was verified by western blot analysis by probing for SR, mitochondria, nuclei, and cytoplasm-specific proteins (**Supplementary Figure 7**). Western blot analyses of SR-mitochondrial interface-associated proteins show that SLN levels were high, whereas the levels of SERCA2a and RyR2 were significantly low in the MAMs of *mdx:utrn<sup>-/-</sup>* ventricles (**Figure 6B**). In the MAMs of *mdx:utrn<sup>-/-</sup>:sln<sup>+/-</sup>* ventricles, the SLN level was significantly reduced, whereas SERCA2a and RyR2 levels remained low and not significantly

different from those of *mdx:utrn*<sup>-/-</sup> ventricles (**Figure 6B**). PLN levels were unaltered between the MAMs of WT, *mdx:utrn*<sup>-/-</sup> and *mdx:utrn*<sup>-/-</sup>:*sln*<sup>+/-</sup> ventricles (**Figure 6B**).

LC-MS/MS-based proteomic profiling of MAMs identified a total of 2300 proteins across WT, *mdx:utrn*<sup>-/-</sup> and *mdx:utrn*<sup>-/-</sup>:*sln*<sup>+/-</sup> mice groups. Gene Ontology (GO) term mapping analysis was performed on the batch-corrected total proteins identified to parse the list based on their subcellular localization. The total number of proteins, as well as proteins pertaining to mitochondrial and SR localizations, were not significantly different among the three groups (**Supplementary Figure 8**). However, there were 159 and 82 individual proteins that differed significantly ( $p < 0.05$ ) between WT and *mdx:utrn*<sup>-/-</sup> mice and between *mdx:utrn*<sup>-/-</sup> and *mdx:utrn*<sup>-/-</sup>:*sln*<sup>+/-</sup> mice, respectively. As shown by the Venn diagram (**Figure 6C**), there were 43 proteins altered in both comparisons i.e., WT versus *mdx:utrn*<sup>-/-</sup> MAMs as well as *mdx:utrn*<sup>-/-</sup> versus *mdx:utrn*<sup>-/-</sup>:*sln*<sup>+/-</sup> MAMs (**Figure 6D**). These included 30 proteins that were down-regulated and 13 proteins that were up-regulated in the MAMs of *mdx:utrn*<sup>-/-</sup> ventricles compared to those of WT mice. All 43 proteins were reversibly altered in *mdx:utrn*<sup>-/-</sup> versus *mdx:utrn*<sup>-/-</sup>:*sln*<sup>+/-</sup> MAMs. Hierarchical clustering of these 43 shared proteins revealed restoration to WT levels in the MAMs of *mdx:utrn*<sup>-/-</sup>:*sln*<sup>+/-</sup> ventricles, such that *mdx:utrn*<sup>-/-</sup>:*sln*<sup>+/-</sup> and WT MAMs represented a single cluster, indistinguishable from one another and clustered apart from *mdx:utrn*<sup>-/-</sup> MAMs (**Figure 6D**). Ingenuity® Pathway Analysis (IPA) of the significantly altered proteins ( $p=0.05$ ) revealed that metabolic pathways involved in mitochondrial function, such as fatty acid oxidation I, and TCA cycle II, were downregulated in the MAMs of *mdx:utrn*<sup>-/-</sup> ventricles, whereas these same pathways were upregulated in the MAMs of *mdx:utrn*<sup>-/-</sup>:*sln*<sup>+/-</sup> ventricles (**Figure 6E**).

## DISCUSSION

Abnormal  $\text{Ca}^{2+}_i$  cycling is one of the major disease-causing mechanisms in DMD (4-8). Chronic accumulation of cytoplasmic  $\text{Ca}^{2+}$  could force mitochondria to uptake more  $\text{Ca}^{2+}$  and increase  $\text{Ca}^{2+}_m$  concentration, which further contributes to mitochondrial dysfunction and myofiber necrosis (7, 10, 11). In support of this notion, preventing mitochondrial dysfunction is shown to partially rescue the muscular dystrophy phenotype (23-25). However, the molecular mechanism(s) that contribute to  $\text{Ca}^{2+}_m$  overload and mitochondrial dysfunction in dystrophic myocardium is not fully understood. The findings from the current study indicate that SLN upregulation contributes significantly to mitochondrial dysfunction in the myocardium of *mdx:utrn*<sup>-/-</sup> mice. Our studies specifically demonstrated that reducing SLN expression can (1) improve SR  $\text{Ca}^{2+}$  handling and prevent  $\text{Ca}^{2+}_m$  overload, (2) prevent  $\Delta\Psi_m$  loss, (3) improve mitochondrial respiration, (4) reduce mitochondrial cristae loss, and (5) improve SR-mitochondria interaction in the myocardium of *mdx:utrn*<sup>-/-</sup> mice.

Consistent with the *mdx* model (18), cardiac myocytes from *mdx:utrn*<sup>-/-</sup> mice show dysregulated  $\text{Ca}^{2+}_i$  handling, as evidenced by increased twitch- $\text{Ca}^{2+}$  transients, decreased SR  $\text{Ca}^{2+}$  uptake, increased SR  $\text{Ca}^{2+}$  leak, defective  $\text{Ca}^{2+}$  removal from the cytosol and SR  $\text{Ca}^{2+}$  overload. In addition, we found increased levels of  $\text{Ca}^{2+}_m$  content in the dystrophic cardiac myocytes. Intriguingly, reducing SLN expression not only improved the SR  $\text{Ca}^{2+}$  cycling but also reduced  $\text{Ca}^{2+}_m$  overload in dystrophic myocytes. These findings suggest that improving SERCA function via SLN reduction can prevent chronic accumulation of cytoplasmic  $\text{Ca}^{2+}$  and thereby reduce  $\text{Ca}^{2+}_m$  uptake in the dystrophic myocardium. In support of this, both reduction and ablation of SLN improved SERCA function, as well as reduced  $\text{Ca}^{2+}_m$  load in skeletal muscles of *mdx* mice (19).

Molecular mechanisms causing  $\text{Ca}^{2+}_m$  overload in dystrophic cardiac myocytes are not fully understood. NCLX, which is involved in mitochondrial  $\text{Ca}^{2+}$  efflux (26) is significantly

higher in the *mdx* heart mitochondria (27). However, NCLX protein levels in the hearts of *mdx:utrn*<sup>-/-</sup> mice remain unchanged. In addition, the protein levels of LETM1, a mitochondrial Ca<sup>2+</sup>/H<sup>+</sup> antiporter involved in Ca<sup>2+</sup><sub>m</sub> sequestration at a low increase in Ca<sup>2+</sup> (28) were not altered in the myocardium of *mdx:utrn*<sup>-/-</sup> mice compared to that of WT controls. Furthermore, reducing SLN expression did not affect the expression levels of these proteins in the dystrophic myocardium, suggesting that these proteins may not contribute to the Ca<sup>2+</sup><sub>m</sub> overload in the cardiac myocytes of *mdx:utrn*<sup>-/-</sup> mice.

MCU, a Ca<sup>2+</sup> selective channel (29), and its modulator, MICU1 (30, 31) are shown to express at higher levels in *mdx* hearts and have been linked to increased Ca<sup>2+</sup><sub>m</sub> uptake (32, 33). In *mdx:utrn*<sup>-/-</sup> myocardium, we found elevated levels of MCU but significantly lower levels of MICU1. Despite the low Ca<sup>2+</sup><sub>m</sub> content, MCU levels remained high in the *mdx:utrn*<sup>-/-</sup>:*sln*<sup>+/-</sup> ventricles, whereas MICU1 levels increased. MICU1 has been shown to play a dual role in MCU regulation, acting as an inhibitor at low cytoplasmic Ca<sup>2+</sup> concentration and an activator at high cytoplasmic Ca<sup>2+</sup> concentration (31, 34). We, therefore, speculate that increasing MCU levels could result in increased Ca<sup>2+</sup><sub>m</sub> content in dystrophic myocytes. On the other hand, changes in MICU1 levels could be compensatory in *mdx:utrn*<sup>-/-</sup> and *mdx:utrn*<sup>-/-</sup>:*sln*<sup>+/-</sup> myocytes as a means of normalizing Ca<sup>2+</sup><sub>m</sub> load. The functional relevance of the differential expression of MCU and MICU1 in regulating Ca<sup>2+</sup><sub>m</sub> uptake in *mdx:utrn*<sup>-/-</sup> and *mdx:utrn*<sup>-/-</sup>:*sln*<sup>+/-</sup> myocardium, however, remains to be expanded by future studies.

Several studies have reported impaired oxidative phosphorylation, elevated reactive oxygen species (ROS) generation, impaired mitochondrial respiration, and reduced ATP production in skeletal and cardiac muscles of *mdx* mice and skeletal muscle biopsies from DMD patients (12, 13, 33, 35-38). We found no difference in the protein levels of electron transport chain

protein subunits or individual mitochondrial complex activities in the hearts of *mdx:utrn*<sup>-/-</sup> mice. Our findings are also consistent with previously reported unchanged mitochondrial complex activities in the skeletal muscles of *mdx:utrn*<sup>-/-</sup> mice (39). Furthermore, there was no difference in protein oxidation and carbonylation, and the protein level of MnSOD suggests that oxidative stress may not play a significant role in mitochondrial dysfunction in *mdx:utrn*<sup>-/-</sup> hearts. However, to validate this notion, direct measurement of ROS, measurement of other antioxidants, and NADPH oxidase pathways need to be studied in these hearts. In the absence of oxidative stress and unchanged complex activities, loss of  $\Delta\Psi_m$  might significantly contribute to decreased mitochondrial respiration in the cardiac myocytes of *mdx:utrn*<sup>-/-</sup> mice. In support of this, there is a decrease in  $\Delta\Psi_m$  and impaired mitochondrial respiration in the *mdx:utrn*<sup>-/-</sup> cardiac myocytes. Excessive accumulation of  $Ca^{2+}$  in mitochondria leads to functional impairments, which could lead to decreased  $\Delta\Psi_m$  (40). Thus, SLN reduction improved  $\Delta\Psi_m$  and mitochondrial function in *mdx:utrn*<sup>-/-</sup> cardiac myocytes by reducing  $Ca^{2+}_m$  overload.

In skeletal muscles, SLN overexpression is shown to uncouple the SERCA pump as well as induce mitochondrial biogenesis and enhance energy metabolism (41). However, in dystrophic myocardium, SLN overexpression could uncouple the SERCA pump from  $Ca^{2+}$  transport, resulting in the accumulation of  $Ca^{2+}$  in the cytoplasm and increased ATP utilization. This could further increase the cytoplasmic  $Ca^{2+}$  load and cause an increase in energy demand, leading to increased  $Ca^{2+}_m$  uptake, loss of  $\Delta\Psi_m$ , and mitochondrial dysfunction. This is supported by the increased loss of mitochondrial cristae, a membrane hub where most of the respiratory complexes embed to account for oxidative phosphorylation and ATP synthesis in the *mdx:utrn*<sup>-/-</sup> myocytes. In support of this idea, reducing SLN expression improved SERCA function, reduced  $Ca^{2+}_m$  overload, prevented the loss of  $\Delta\Psi_m$ , and improved mitochondrial cristae structure and respiration in

dystrophic myocardium. Reducing or abolishing SLN expression also prevents  $\text{Ca}^{2+}_m$  overload and improves metabolism in the muscles of *mdx* mice (19). Thus, reducing SLN expression in dystrophic muscles is rather beneficial and improves mitochondrial function.

Electron micrographs of ventricular tissues from *mdx:utrn*<sup>-/-</sup> mice revealed a large number of smaller mitochondria, as evidenced by an increased number of mitochondria with a smaller surface area, indicating impaired mitochondrial dynamics. Furthermore, mitochondrial copy number is significantly reduced in *mdx:utrn*<sup>-/-</sup> ventricles indicating defects in mitochondrial fission and fusion cycles. Although SLN reduction did not normalize mitochondrial copy number, it did improve mitochondrial number, surface area, and aspect ratio in *mdx:utrn*<sup>-/-</sup> ventricles. These findings suggest that reducing SLN expression could partially restore mitochondrial dynamics. It is also worth mentioning that SLN reduction restores autophagy and mitochondrial dynamics in dystrophic dog myotubes (42). Our future studies will address the molecular mechanisms associated with mitochondrial dynamics in the *mdx:utrn*<sup>-/-</sup>:*sln*<sup>+/-</sup> myocardium.

A growing number of studies suggest that a proper ER/SR-mitochondrial interface is required for mitochondrial function (43). Recent studies also indicate that ER/mitochondrial junctions are disrupted in the heart (33) and muscles (44) of *mdx* mice. However, there are no studies on the interaction of SR and mitochondria, although SR is the major regulator of cytosolic  $\text{Ca}^{2+}$  in the heart during excitation-contraction coupling. For the first time, our findings show that cristae density loss in SR-opposed mitochondria is significantly greater than in non-SR-opposed mitochondria in *mdx:utrn*<sup>-/-</sup> ventricles. Furthermore, we found increased levels of SLN, decreased levels of SR  $\text{Ca}^{2+}$  uptake (SERCA2a), and release (RyR) proteins as well as decreased levels of proteins involved in mitochondrial metabolism in the MAMs of *mdx:utrn*<sup>-/-</sup> myocardium. These findings suggest that SR-mitochondrial interactions are significantly impaired in the *mdx:utrn*<sup>-/-</sup>



myocardium. The increased SERCA2a/SLN ratio in the MAMs of *mdx:utrn*<sup>-/-</sup> myocardium suggests that SLN could directly inhibit the SERCA pump in MAMs. In addition, SLN may enhance the inhibitory effect of PLN (45), another key regulator of SERCA2a that is unaltered in the MAMs of *mdx:utrn*<sup>-/-</sup> myocardium. Thus, SLN enrichment in the MAMs, which has not been previously reported, could result in decreased SERCA function and increased Ca<sup>2+</sup> accumulation at the SR-mitochondrial junction, forcing the mitochondria to uptake more Ca<sup>2+</sup> and causing mitochondrial dysfunction and damage. The fact that SLN haploinsufficiency results in reduced levels of SLN in the MAMs, reduced Ca<sup>2+</sup><sub>m</sub> content, and improved mitochondrial structure and function in the ventricles of *mdx:utrn*<sup>-/-</sup>:*sln*<sup>+/-</sup> mice validates this idea. It is also worth noting that the total SERCA2a, PLN, and RyR levels are unaffected in the *mdx:utrn*<sup>-/-</sup> ventricles, and SLN reduction or ablation do not affect the expression of these proteins (**Supplementary Figure 3**) (17).

Proteomic analyses show the enrichment of proteins involved in the metabolic pathways and mitochondrial function in the MAMs of *mdx:utrn*<sup>-/-</sup>:*sln*<sup>+/-</sup> myocardium. Although elucidation of the underlying changes in MAMs that drive the salutary effects of SLN reduction in the setting of DMD is beyond the scope of this study, results gleaned from proteomic profiling of MAMs provide valuable insights for future mechanistic investigation. Frataxin (FXN), for instance, which functions in regulating mitochondrial iron transport and respiration, was reduced in dystrophic MAMs, and restored by SLN reduction (**Figure 6D**). Lack of FXN is known to cause mitochondrial dysfunction and Friedreich's ataxia, a recessive neurodegenerative disorder commonly associated with hypertrophic cardiomyopathy (46). Thus, there may be a potential association between FXN reduction in the MAMs and mitochondrial dysfunction and cardiomyopathy in DMD. Similarly, mitochondrial methionyl-tRNA synthetase 2 (Mars2) protein,

which stimulates mitochondrial  $\text{Ca}^{2+}$  influx via direct interaction with MCU (47), was restored to normal levels in *mdx:utrn<sup>-/-</sup>:sln<sup>+/-</sup>* MAMs (**Figure 6D**) and might thus contribute to the observed improvements in  $\text{Ca}^{2+}_m$  handling in the ventricles of *mdx:utrn<sup>-/-</sup>:sln<sup>+/-</sup>* mice. Likewise, several proteins that were diminished in dystrophic MAMs and rescued by SLN knockdown could contribute to observed improvements in mitochondrial structure and function. Our future studies are aimed at dissecting the roles of these altered proteins in DMD, particularly the normative effects of SLN depletion and how SLN orchestrates mitochondrial dynamics.

In summary, our data reveal that reducing SLN expression is sufficient to restore cardiac SERCA function and subsequently  $\text{Ca}^{2+}_i$  handling in dystrophic myocardium. These changes can further improve SR/mitochondrial interaction, prevent  $\text{Ca}^{2+}_m$  overload and loss of  $\Delta\Psi_m$ , and reduce mitochondrial structural damage and adverse cardiac remodeling, thereby delaying the progression of cardiomyopathy. Current findings not only advance our understanding of the molecular mechanisms associated with mitochondrial dysfunction in dystrophic myocardium but also add a new dimension to the therapeutic exploration of reducing or inhibiting SLN function in preventing cardiomyopathy in DMD patients.

## METHODS

**Sex as a biological variable.** We used only 3-4-month-old male mice for this study because of the X-linked inheritance of DMD and its potential relevance to human patients, as well as the difficulty in breeding these mice to obtain a large number of mice of both sexes.

**Mouse models-** The *mdx:utrn<sup>-/-</sup>:sln<sup>+/-</sup>* mice were generated by crossing the *mdx:utrn<sup>+/-</sup>* mice to *sln<sup>-/-</sup>* mice (17). These mice were crossed for five generations to obtain the *mdx:utrn<sup>+/-</sup>:sln<sup>+/-</sup>* mice in an isogenic background. The male and female *mdx:utrn<sup>+/-</sup>:sln<sup>+/-</sup>* mice were then crossed to generate the *mdx:utrn<sup>-/-</sup>* and *mdx:utrn<sup>-/-</sup>:sln<sup>+/-</sup>* mice. The genotypes of the mice were identified by polymerase chain reaction (PCR) using previously published sequences (48, 49). Mice were kept under a 12-hour light/dark cycle with a temperature of 22-24°C and 60-70% humidity and fed ad libitum under a normal chow diet. Animal numbers were predetermined based on pilot studies and sample sizes were similar to those generally employed in the field. No samples, mice, or data points were excluded from the data analysis. Animals were not randomized except for the genotypes. For echocardiography, investigators were blinded to the genotypes.

**Histology-** Five-micron paraffin-embedded myocardial sections were used for standard PSR staining. The collagen fibers stained in red by PSR were calculated using the NIH ImageJ 1.43u program.

**Echocardiography-** Echocardiography was performed on anesthetized (2% isoflurane) mice using a high-resolution ultrasound machine VisualSonic/Vevo 3100 system with a high-frequency transducer (MXT400) (50). The LV systolic function was assessed by measuring LV interventricular septal thicknesses (IVS), LV internal dimensions (LVID), and posterior wall thicknesses (PW) at diastole and systole (IVSd, LVIDd, PWd and IVSs, LVIDs, PWs respectively) from M-mode images at the level of the papillary muscles. LV EF and LV FS were calculated

using the Vevo 3100 software. Additionally, LV diastolic function was evaluated using Pulse Wave Doppler by imaging Transmitral inflow Doppler via an apical 4-chamber view. The Doppler indexes include the E/A ratio, deceleration time (DT) of early filling of mitral inflow, isovolumetric relaxation time (IVRT), and isovolumetric contraction time (IVCT). Doppler parameters such as the E/A ratio and MPI ( $MPI=(IVRT+IVCT)/ET$ ) were calculated to determine the diastolic function and overall myocardial performance.

**Ca<sup>2+</sup> transient measurements-** Cardiac myocytes were enzymatically isolated from mouse ventricles following Langendorff heart perfusions as described previously(51, 52). Ca<sup>2+</sup> transient amplitude and SR Ca<sup>2+</sup> content were measured in isolated cardiac myocytes using Ca<sup>2+</sup> indicator Fluo-4, AM (Molecular Probes F14201) at 34–36°C, as described earlier (18). Briefly, myocytes were loaded with Fluo-4 AM, and field stimulated at 0.5 Hz to maintain consistent SR Ca<sup>2+</sup> load. The fluorescence was excited at ~485 nm and the emissions were measured at ~530 nm using a Nikon Eclipse TE200 inverted microscope. Fluorescence intensity was measured as the ratio of the fluorescence (F) over the basal diastolic fluorescence (F<sub>0</sub>). The amplitude of the caffeine (10 mmol/liter) induced Ca<sup>2+</sup> transient was used as a measure of total SR Ca<sup>2+</sup> content. Fractional SR Ca<sup>2+</sup> release was calculated by dividing the height of the last twitch transient by the height of the caffeine transient.

**Mitochondrial Ca<sup>2+</sup> Efflux-** The Ca<sup>2+</sup><sub>m</sub> efflux was determined as described previously (12, 20). Briefly, cardiac myocytes were loaded with Fluo-4, AM, perfused with normal Tyrode's, and stimulated at 0.5Hz to delineate healthy cells. Followed by perfusion with Li<sup>+</sup> Tyrode's (free of Ca<sup>2+</sup>, and Na<sup>+</sup> and supplemented with glucose) for 30 sec to prevent Ca<sup>2+</sup> release/influx via sodium-calcium exchanger (NCX) and Ca<sup>2+</sup> entry across the plasma membrane. Later, myocytes were perfused with Li<sup>+</sup> Tyrode's containing 1mM tetracaine and 1μM thapsigargin for 30 sec to

block both SR  $\text{Ca}^{2+}$  uptake and release. At this point, myocytes were perfused with  $2\mu\text{M}$  FCCP and  $1\mu\text{g/ml}$  oligomycin for 30 sec along with tetracaine and thapsigargin to deplete the  $\text{Ca}^{2+}_m$ . This  $\text{Ca}^{2+}_m$  release is observed as a slight elevation of cytosolic  $\text{Ca}^{2+}$  and measured as  $\text{Ca}^{2+}_m$  efflux/transients (**Supplementary Figure 4**). The  $F/F_0$  was evaluated as relative  $\text{Ca}^{2+}_m$  content.

**Confocal imaging and  $\text{Ca}^{2+}_m$  measurements-** The  $\text{Ca}^{2+}$  content of mitochondria in isolated myocytes was evaluated using Rhod-2, AM (Cat# R1245MP, Invitrogen). According to the manufacturer's protocols, Rhod-2, AM was reduced just before the experiment using sodium borohydride ( $\text{NaBH}_4$ ) to further enhance mitochondrial localization. Myocytes were loaded with  $5\mu\text{M}$  reduced Rhod-2, AM and incubated at  $37^\circ\text{C}$  for 30 min followed by 3 x 10 min washes. Images were captured using the Nikon A1R confocal microscope at the Rutgers-Confocal Imaging Core Facility, NJMS, and the red fluorescence intensity was calculated using NIH ImageJ software.

**Measurements of mitochondrial membrane potential-** Myocytes were loaded with either  $15\mu\text{M}$  JC-1 (Cat# T3168, Invitrogen) or  $100\text{ nM}$  CMXRos (Cat# M7512, Invitrogen) and incubated at  $37^\circ\text{C}$  for 30 min followed by 3 x 10 min washes to remove the excess dye, according to manufacturer's protocol. Later the images were captured using the Nikon A1R confocal microscope at the Rutgers-Confocal Imaging Core Facility, NJMS. The images were then analyzed using NIH ImageJ software to quantify the red/green ratio of the MFI for JC-1 and red MFI for CMXRos.

**Purification of MAMs-** MAMs were purified from fresh ventricular tissues following previously established procedures (53, 54). We pooled 4-5 ventricles for each preparation. In brief, ventricles were washed with ice-cold phosphate-buffered saline (PBS), homogenized in an isolation buffer ( $225\text{ mM}$  mannitol,  $75\text{ mM}$  sucrose,  $0.1\%$  bovine serum albumin,  $10\text{ mM}$  HEPES/Tris,  $100\mu\text{M}$

EGTA/Tris, pH 7.4) containing protease inhibitors and centrifuged at 600 x g for 10 min to pellet down the unbroken cells and nucleus. The supernatant was centrifuged two more times and the final supernatant collected was centrifuged at 10,000 x g for 10 min to pellet down the crude mitochondria. The supernatant containing microsomal (SR/ER) and cytosolic proteins was collected separately and stored at 4°C until further processing. The crude mitochondrial pellet was washed twice to remove any microsomal contamination. Further, the crude mitochondria were suspended in a small volume of isolation buffer, overlaid on Percoll medium (Percoll buffer containing mannitol (400 mg) and sucrose (250 mg) in isolation buffer) and centrifuged at 100,000 x g for 1 hour. The resulting centrifugation forms a top layer of MAMs fraction and a bottom layer of pure mitochondria above the Percoll pellet. The MAMs and mitochondrial fractions were collected into separate tubes and restored to 10 times the volume with an isolation buffer. Both fractions collected were then subjected to 6,300 x g for 10 min to prevent contamination of MAMs in the mitochondrial fraction and mitochondrial contamination in the MAMs. The final mitochondrial pellet was resuspended in an isolation buffer. The supernatant resulting from centrifuging the MAMs fraction was further subjected to 100,000 x g for 1 hour. to pellet the pure MAMs. The supernatant containing microsomal (SR/ER) and cytosolic proteins was centrifuged at 20,000 x g for 30 min to remove mitochondrial and lysosomal contamination. The supernatant was further centrifuged at 100,000 x g for 1 hour. The resulting pellet contains an SR/ER fraction, and the supernatant is considered a cytosolic fraction.

**Seahorse measurements-** Mitochondria were isolated as described in MAMs purification and subjected to complex II-driven mitochondrial respiration using Seahorse XFe24 Analyzer (55, 56). Briefly, the mitochondrial pellet was re-suspended in mitochondrial assay buffer 1 (MAS1 - 220 mM D-Mannitol, 70 mM sucrose, 10 mM KH<sub>2</sub>PO<sub>4</sub>, 5 mM MgCl<sub>2</sub>, 2 mM HEPES, 1 mM EGTA,

and 0.2% (w/v) of fatty acid-free BSA, pH, 7.4 adjusted with KOH). The protein concentration was estimated using a Bradford assay kit (Bio-Rad). After estimation, the mitochondria were pelleted again and resuspended in mitochondrial assay buffer 2 (MAS2; MAS1 containing 10 mM succinate and 2  $\mu$ M rotenone). About 5  $\mu$ g of mitochondria in 100  $\mu$ l of MAS2 was added to each well of the Seahorse XFe 24 plate and centrifuged at 2000 X g for 20 min at 4<sup>o</sup> C. After verifying proper adherence of mitochondria, 400 $\mu$ L of pre-warmed (37<sup>o</sup>C), MAS1 with 5mM ADP was added to each well and the state III mitochondrial respiration was measured. Mitochondria were then treated with oligomycin (3.2  $\mu$ M), FCCP (4  $\mu$ M), and antimycin (4  $\mu$ M). Seahorse protocol was followed, however, after each injection, two measurements were made to determine the oxygen consumption rate (OCR), extracellular acidification rate (ECAR), and various states of respiration (State III, State IV<sub>0</sub>, State III <sub>$\mu$</sub> ) (55). State III respiration represents the formation of ATP from ADP and inorganic phosphate, State IV<sub>0</sub> respiration represents the proton leak due to the inhibition of the ATP synthase by oligomycin and State III <sub>$\mu$</sub>  respiration represents the status of maximal respiratory capacity after FCCP treatment. Further, the RCR an index of mitochondrial coupling was calculated by dividing the values of State III/State IV<sub>0</sub> (55, 56).

**Western blot analysis-** Total protein extraction and western blotting were carried out as described before (17). Briefly, after protein transfer, the nitrocellulose membranes were stained with Ponceau S and cut into strips based on the molecular weight of each protein studied. The membrane strips were then blocked with 3% milk in phosphate-buffered saline (PBS) and probed overnight at 4<sup>o</sup> C using antibodies specific for SLN (anti-rabbit, 1:3000, custom made) (57), PLN (anti-rabbit, 1:5000, custom made) (57), RyR2 (anti-rabbit, 1:1000, ThermoFisher Scientific, PA5-77717), SERCA2a (anti-rabbit, 1:5000, custom made) (57), mitochondrial Ca<sup>2+</sup> uniporter (MCU; anti-rabbit, 1:1000, CST, #149973), mitochondrial Ca<sup>2+</sup> uptake 1 (MICU1; anti-rabbit, 1:1000, CST,

#12524), NCXL (anti-rabbit, 1:1000, ThermoFisher Scientific, PA5-114330), LETM1 (anti-rabbit, 1:1000, ABclonal, #A15685), TRPC1 (anti-rabbit, 1:1000, Abcam, #ab192031), total oxidative phosphorylation subunits cocktail (OXPHOS subunits; anti-mouse, 1:10000, Abcam, #ab110413), 4-HNE (anti-rabbit, 1:3000, Abcam, #ab46545), SOD2 (anti-mouse, 1:1000, Santacruz, #sc-137254), long-chain fatty-acid-coenzyme A ligase 4 (FACL4/ACSL4, anti-mouse, 1:1000, Santacruz, #sc-365230), glucose-regulated protein 75 (Grp75, anti-rabbit, 1:1000, CST, #3593),  $\alpha$ -tubulin (anti-mouse, 1:5000, Sigma-Aldrich, #T6199), lamin A/C (4C11, anti-mouse, 1:1000, CST, #4777S) and cytochrome c oxidase IV (COX IV; anti-rabbit, 1:1000, CST, #4850T). Membranes were incubated with appropriate secondary antibodies for 1 hour at room temperature and visualized with a SuperSignal West Dura Substrate kit (ThermoFisher Scientific) using BioRad ChemiDoc MP Imaging System. Quantitation of signals was performed using Image Lab version 5.1 software and normalized to Ponceau S staining.

To detect the oxidative modification of proteins, total or mitochondrial protein fractions from the ventricles were derivatized using an OxyBlot protein oxidation detection kit (Cat. #S7150, Millipore), separated on 12% SDS-PAGE and transferred to nitrocellulose membrane. The stable dinitrophenyl (DNP) proteins were detected by immunoblot using anti-DNP antibodies. Quantitation of signals was performed using Image Lab v. 5.1 software and normalized to Ponceau S staining.

**Complex activity assays-** The mitochondrial complex I (NADH-dehydrogenase) and complex IV (cytochrome c oxidase) activities were measured in freshly prepared ventricular tissue lysates using Abcam assay kits (complex I, No. ab109721; complex IV, No. ab109911) as per the manufacturer's instructions. For complex I activity, the optical density was measured at 450 nm



in kinetic mode at room temperature (RT) for 30 min, and for complex IV activity, the optical density was measured at 550 nm in kinetic mode at RT for 120 min.

**Mitochondrial copy number-** Mitochondrial DNA copy number was calculated as the ratio of mitochondrial genome to nuclear genome following real-time quantitative PCR using total DNA as described before (19, 58). Briefly, total DNA was prepared from the ventricular tissues using the Monarch Genomic DNA purification Kit (New England Biolabs; T3010). The qPCR was performed using primers specific for mouse mitochondrial DNA (forward 5'-CTAGAAACCCCGAAACCAA -3'; reverse, 5'-CCAGCTATCACCAAGCTCGT-3') and nuclear DNA (beta 2-microglobulin; forward, 5'- ATGGGAAGCCGAACATACTG-3'; reverse 5'- CAGTCTCAGTGGGGGTGAAT-3').

**Electron microscopy-** Transmission electron microscopy (TEM) was performed as described previously (59). Briefly, ventricular tissues were fixed overnight in Karnovsky's solution (2% paraformaldehyde/2.5% glutaraldehyde in 0.1M phosphate buffer). The fixed samples were then processed at the Rutgers Core Imaging Lab at Robert Wood Johnson Medical School, NJ. After post-fixation with 1% Osmium Tetroxide in PBS for 1 hour, the tissue was dehydrated with a graded series of acetone concentrations and embedded in Spar resin. Sections of 98 nm thickness were placed on copper grids that were double stained with uranyl acetate and lead citrate and examined under JEOL 1200 electron microscope. Images were captured and analyzed using NIH Image J software.

**Proteomics and data analysis-** Purified MAMs were resolved on 4-20% Bio-Rad Mini-PROTEAN TGX precast gradient gels and subjected to LC-MS/MS on a Thermo Scientific Orbitrap Fusion Lumos Tribrid mass spectrometer (Lumos MS) at Rutgers Center for Advanced Proteomics Research facility. Three replicate experiments were performed in two batches. The

resulting MS/MS spectra were searched against a SwissProt mouse database using the Sequest search engine on the Proteome Discoverer (V2.4) platform using a protein false discovery rate (FDR) of less than 1%. The ratios between *mdx:utrn*<sup>-/-</sup> and WT and between *mdx:utrn*<sup>-/-</sup>:*sln*<sup>+/-</sup> and WT were calculated using the spectra counting method. In addition to ratio calculations, Partek Genomics Suite 7.0 was used for batch correction of raw spectral counts, followed by quantile normalization, pairwise comparisons using one-way analysis of variance (ANOVA), hierarchical clustering, and principal components analysis (PCA). Those proteins with a significant spectral count ratio > 2, multiple hypothesis-corrected *P*-value < 0.05, and fold-difference > 1.5 were considered as most significantly different. GO Term Mapper was used to determine the sub-cellular localization of the various proteins identified, and Ingenuity® Pathway Analysis (IPA) Software (Qiagen) was used for functional analysis, including enriched biological processes, pathways, and upstream regulators.

**Statistical analysis-** The data were analyzed in an unbiased and blinded manner to ensure that these results are consistent and reproducible. Each western blotting experiment was repeated two or three times, and the mean values of these repeated experiments were used for quantitation. All statistical analyses were performed using GraphPad Prism v6.01 software. Ordinary one-way ANOVA was used for multi-group comparison. Data were presented as mean ±SEM. *P*<0.05 was considered significant.

**Study Approval -** All animal procedures were approved by the Institutional Animal Care and Use Committee (IACUC) of New Jersey Medical School (NJMS), Rutgers, Newark according to the Guide to the Care and Use of Laboratory Animals published by the United States National Institute of Health (NIH, 8<sup>th</sup> Edition, 2011).

**Data availability-** All data presented in this article are included in the main text, supplementary figures, and Supporting Data Values file. Any additional requests can be made to the corresponding author.

## **AUTHOR CONTRIBUTIONS**

G.J.B and S.M conceived and designed research; S.M., N.F., C.L.G., G.P., and R.M. analyzed data; S.M., L-H.X., C.L.G., J.S., and G.J.B interpreted results; S.M. and G.J.B drafted the manuscript; S.M., L-H.X., C.L.G., J.S., and G.J.B edited the manuscript; S.M., N.F., C.G., G.P., R.M., J.S., L-H.X., and G.J.B approved the final version of the manuscript.

## **ACKNOWLEDGMENTS**

This work was supported by the National Institute of Arthritis and Musculoskeletal and Skin Diseases Grant AR069107 (to G.J.B.). L.H.X was supported by the National Heart, Lung, and Blood Institute grants, R01HL133294 and R01HL157116. C.L.G. was supported by the American Heart Association grant (18IPA3417002). Vevo 3100 High-Resolution Imaging System was supported by S10 Instrumentation grant, S10OD025238.

## REFERENCES

1. Bushby K, et al. Diagnosis and management of Duchenne muscular dystrophy, part 1: diagnosis, and pharmacological and psychosocial management. *Lancet Neurol.* 2010;9(1):77-93.
2. Duan D, et al. Duchenne muscular dystrophy. *Nat Rev Dis Primers.* 2021;7(1):13.
3. Woods WA, et al. Emergency department care of patients with Duchenne muscular dystrophy. *Am J Emerg Med.* 2022;60:101-5.
4. Mareedu S, et al. Abnormal Calcium Handling in Duchenne Muscular Dystrophy: Mechanisms and Potential Therapies. *Front Physiol.* 2021;12:647010.
5. Schultz TI, et al. Cardiovascular Disease in Duchenne Muscular Dystrophy: Overview and Insight Into Novel Therapeutic Targets. *JACC Basic Transl Sci.* 2022;7(6):608-25.
6. Law ML, et al. Dysregulation of Calcium Handling in Duchenne Muscular Dystrophy-Associated Dilated Cardiomyopathy: Mechanisms and Experimental Therapeutic Strategies. *J Clin Med.* 2020;9(2).
7. Budzinska M, et al. The role of mitochondria in Duchenne muscular dystrophy. *J Physiol Pharmacol.* 2021;72(2).
8. Dubinin MV, and Belosludtsev KN. Ion Channels of the Sarcolemma and Intracellular Organelles in Duchenne Muscular Dystrophy: A Role in the Dysregulation of Ion Homeostasis and a Possible Target for Therapy. *Int J Mol Sci.* 2023;24(3).
9. Williams GS, et al. Mitochondrial calcium and the regulation of metabolism in the heart. *J Mol Cell Cardiol.* 2015;78:35-45.
10. Matuz-Mares D, et al. Mitochondrial Calcium: Effects of Its Imbalance in Disease. *Antioxidants (Basel).* 2022;11(5).

11. Robichaux DJ, et al. Mitochondrial permeability transition pore-dependent necrosis. *J Mol Cell Cardiol.* 2023;174:47-55.
12. Kyrychenko V, et al. Mitochondrial dysfunctions during progression of dystrophic cardiomyopathy. *Cell Calcium.* 2015;58(2):186-95.
13. Kang C, et al. Deficit in PINK1/PARKIN-mediated mitochondrial autophagy at late stages of dystrophic cardiomyopathy. *Cardiovasc Res.* 2018;114(1):90-102.
14. Rosenberg P. VDAC2 as a novel target for heart failure: Ca(2+) at the sarcomere, mitochondria and SR. *Cell Calcium.* 2022;104:102586.
15. Hulsurkar MM, et al. Targeting calcium-mediated inter-organellar crosstalk in cardiac diseases. *Expert Opin Ther Targets.* 2022;26(4):303-17.
16. Schneider JS, et al. Increased sarcolipin expression and decreased sarco(endo)plasmic reticulum Ca<sup>2+</sup> uptake in skeletal muscles of mouse models of Duchenne muscular dystrophy. *J Muscle Res Cell Motil.* 2013;34(5-6):349-56.
17. Voit A, et al. Reducing sarcolipin expression mitigates Duchenne muscular dystrophy and associated cardiomyopathy in mice. *Nat Commun.* 2017;8(1):1068.
18. Mareedu S, et al. Sarcolipin haploinsufficiency prevents dystrophic cardiomyopathy in mdx mice. *Am J Physiol Heart Circ Physiol.* 2021;320(1):H200-H10.
19. Balakrishnan R, et al. Reducing sarcolipin expression improves muscle metabolism in mdx mice. *Am J Physiol Cell Physiol.* 2022;322(2):C260-C74.
20. Zhao Z, et al. Modulation of intracellular calcium waves and triggered activities by mitochondrial Ca flux in mouse cardiomyocytes. *PLoS One.* 2013;8(11):e80574.
21. Goetzman E, et al. Complex II Biology in Aging, Health, and Disease. *Antioxidants (Basel).* 2023;12(7).

22. Pendergrass W, et al. Efficacy of MitoTracker Green and CMXRosamine to measure changes in mitochondrial membrane potentials in living cells and tissues. *Cytometry A*. 2004;61(2):162-9.
23. Reutenauer J, et al. Investigation of Debio 025, a cyclophilin inhibitor, in the dystrophic mdx mouse, a model for Duchenne muscular dystrophy. *Br J Pharmacol*. 2008;155(4):574-84.
24. Schiavone M, et al. Alisporivir rescues defective mitochondrial respiration in Duchenne muscular dystrophy. *Pharmacol Res*. 2017;125(Pt B):122-31.
25. Millay DP, et al. Genetic and pharmacologic inhibition of mitochondrial-dependent necrosis attenuates muscular dystrophy. *Nat Med*. 2008;14(4):442-7.
26. Garbincius JF, and Elrod JW. Mitochondrial calcium exchange in physiology and disease. *Physiol Rev*. 2022;102(2):893-992.
27. Dubinin MV, et al. Transport of Ca(2+) and Ca(2+)-dependent permeability transition in heart mitochondria in the early stages of Duchenne muscular dystrophy. *Biochim Biophys Acta Bioenerg*. 2020;1861(10):148250.
28. Waldeck-Weiermair M, et al. Leucine zipper EF hand-containing transmembrane protein 1 (Letm1) and uncoupling proteins 2 and 3 (UCP2/3) contribute to two distinct mitochondrial Ca<sup>2+</sup> uptake pathways. *J Biol Chem*. 2011;286(32):28444-55.
29. Drago I, et al. Mitochondrial Ca<sup>2+</sup> uptake contributes to buffering cytoplasmic Ca<sup>2+</sup> peaks in cardiomyocytes. *Proc Natl Acad Sci U S A*. 2012;109(32):12986-91.
30. Perocchi F, et al. MICU1 encodes a mitochondrial EF hand protein required for Ca(2+) uptake. *Nature*. 2010;467(7313):291-6.

31. Csordas G, et al. MICU1 controls both the threshold and cooperative activation of the mitochondrial Ca<sup>2+</sup>(+) uniporter. *Cell Metab.* 2013;17(6):976-87.
32. Dubinin MV, et al. Duchenne muscular dystrophy is associated with the inhibition of calcium uniport in mitochondria and an increased sensitivity of the organelles to the calcium-induced permeability transition. *Biochim Biophys Acta Mol Basis Dis.* 2020;1866(5):165674.
33. Angebault C, et al. Metformin Reverses the Enhanced Myocardial SR/ER-Mitochondria Interaction and Impaired Complex I-Driven Respiration in Dystrophin-Deficient Mice. *Front Cell Dev Biol.* 2020;8:609493.
34. Matesanz-Isabel J, et al. Functional roles of MICU1 and MICU2 in mitochondrial Ca<sup>2+</sup> uptake. *Biochim Biophys Acta.* 2016;1858(6):1110-7.
35. Kuznetsov AV, et al. Impaired mitochondrial oxidative phosphorylation in skeletal muscle of the dystrophin-deficient mdx mouse. *Mol Cell Biochem.* 1998;183(1-2):87-96.
36. Rybalka E, et al. Defects in mitochondrial ATP synthesis in dystrophin-deficient mdx skeletal muscles may be caused by complex I insufficiency. *PLoS One.* 2014;9(12):e115763.
37. Jung C, et al. Dystrophic cardiomyopathy: amplification of cellular damage by Ca<sup>2+</sup> signalling and reactive oxygen species-generating pathways. *Cardiovasc Res.* 2008;77(4):766-73.
38. Sperl W, et al. High resolution respirometry of permeabilized skeletal muscle fibers in the diagnosis of neuromuscular disorders. *Mol Cell Biochem.* 1997;174(1-2):71-8.



39. Pant M, et al. Metabolic dysfunction and altered mitochondrial dynamics in the utrophin-dystrophin deficient mouse model of duchenne muscular dystrophy. *PLoS One*. 2015;10(4):e0123875.
40. Lai L, and Qiu H. The Physiological and Pathological Roles of Mitochondrial Calcium Uptake in Heart. *Int J Mol Sci*. 2020;21(20).
41. Maurya SK, et al. Sarcolipin Signaling Promotes Mitochondrial Biogenesis and Oxidative Metabolism in Skeletal Muscle. *Cell Rep*. 2018;24(11):2919-31.
42. Niranjana N, et al. Sarcolipin overexpression impairs myogenic differentiation in Duchenne muscular dystrophy. *Am J Physiol Cell Physiol*. 2019.
43. Patergnani S, et al. Calcium signaling around Mitochondria Associated Membranes (MAMs). *Cell Commun Signal*. 2011;9:19.
44. Pauly M, et al. ER stress disturbs SR/ER-mitochondria Ca<sup>2+</sup> transfer: Implications in Duchenne muscular dystrophy. *Biochim Biophys Acta Mol Basis Dis*. 2017;1863(9):2229-39.
45. Asahi M, et al. Sarcolipin inhibits polymerization of phospholamban to induce superinhibition of sarco(endo)plasmic reticulum Ca<sup>2+</sup>-ATPases (SERCAs). *J Biol Chem*. 2002;277(30):26725-8.
46. Payne RM. Cardiovascular Research in Friedreich Ataxia: Unmet Needs and Opportunities. *JACC Basic Transl Sci*. 2022;7(12):1267-83.
47. Son J, et al. MARS2 drives metabolic switch of non-small-cell lung cancer cells via interaction with MCU. *Redox Biol*. 2023;60:102628.
48. Grange RW, et al. Fast-twitch skeletal muscles of dystrophic mouse pups are resistant to injury from acute mechanical stress. *Am J Physiol Cell Physiol*. 2002;283(4):C1090-101.

49. Babu GJ, et al. Ablation of sarcolipin enhances sarcoplasmic reticulum calcium transport and atrial contractility. *Proc Natl Acad Sci U S A*. 2007;104(45):17867-72.
50. Vatner DE, et al. Secreted frizzled-related protein 2, a novel mechanism to induce myocardial ischemic protection through angiogenesis. *Basic Res Cardiol*. 2020;115(4):48.
51. Kabaeva Z, et al. Blebbistatin extends culture life of adult mouse cardiac myocytes and allows efficient and stable transgene expression. *Am J Physiol Heart Circ Physiol*. 2008;294(4):H1667-74.
52. Fefelova N, et al. Deficiency of mitochondrial calcium uniporter abrogates iron overload-induced cardiac dysfunction by reducing ferroptosis. *Basic Res Cardiol*. 2023;118(1):21.
53. Wieckowski MR, et al. Isolation of mitochondria-associated membranes and mitochondria from animal tissues and cells. *Nat Protoc*. 2009;4(11):1582-90.
54. Garcia-Perez C, et al. Physical coupling supports the local Ca<sup>2+</sup> transfer between sarcoplasmic reticulum subdomains and the mitochondria in heart muscle. *J Biol Chem*. 2008;283(47):32771-80.
55. Iuso A, et al. Assessing Mitochondrial Bioenergetics in Isolated Mitochondria from Various Mouse Tissues Using Seahorse XF96 Analyzer. *Methods Mol Biol*. 2017;1567:217-30.
56. Sakamuri S, et al. Measurement of respiratory function in isolated cardiac mitochondria using Seahorse XFe24 Analyzer: applications for aging research. *Geroscience*. 2018;40(3):347-56.
57. Babu GJ, et al. Differential expression of sarcolipin protein during muscle development and cardiac pathophysiology. *J Mol Cell Cardiol*. 2007;43(2):215-22.

58. Malik AN, et al. Accurate quantification of mouse mitochondrial DNA without co-amplification of nuclear mitochondrial insertion sequences. *Mitochondrion*. 2016;29:59-64.
59. Guichard JL, et al. Desmin loss and mitochondrial damage precede left ventricular systolic failure in volume overload heart failure. *Am J Physiol Heart Circ Physiol*. 2017;313(1):H32-H45.

## FIGURES

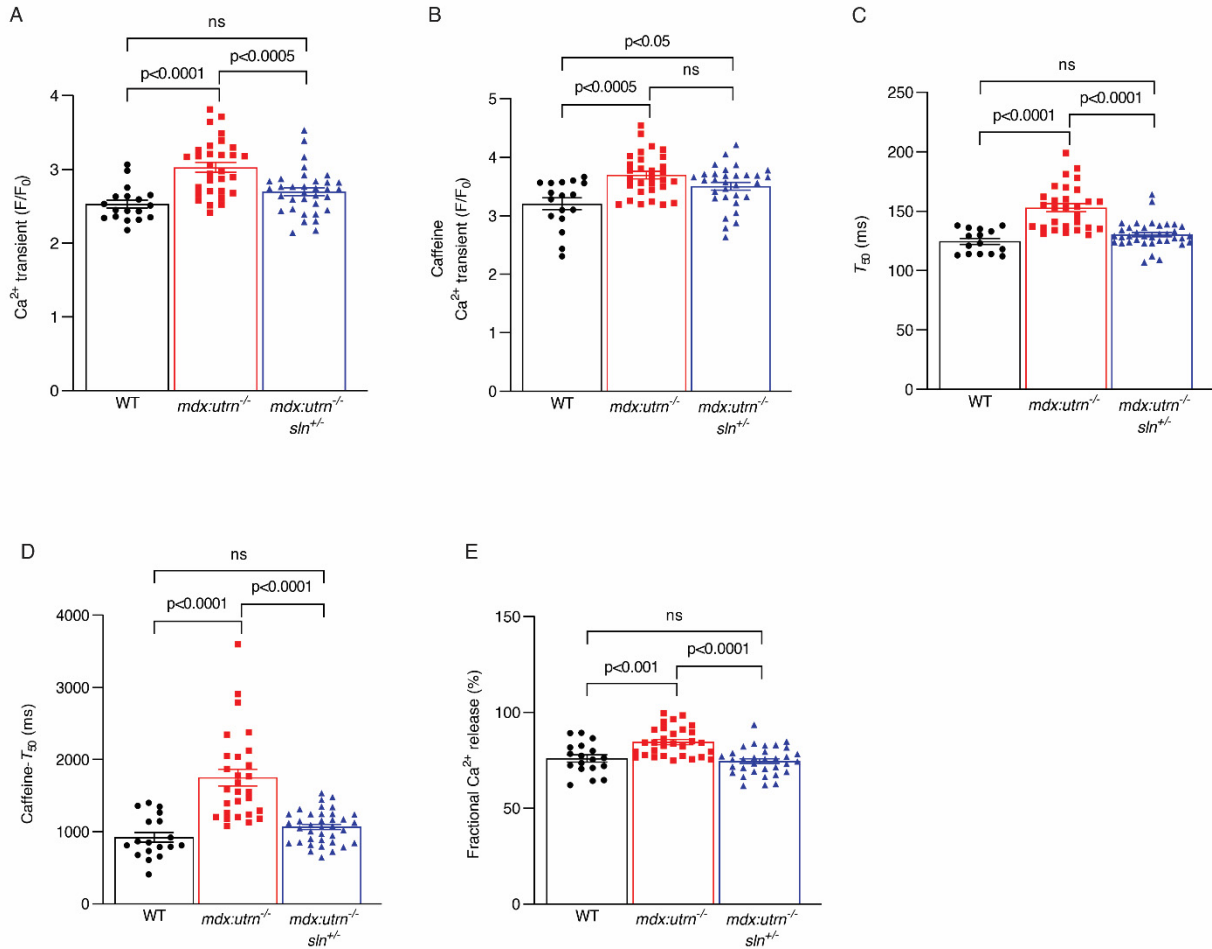


**Figure 1: SR Ca<sup>2+</sup> handling is improved in cardiac myocytes from *mdx:utrn*<sup>-/-</sup>:*sln*<sup>+/-</sup> mice.**

Summarized data for (A) twitch Ca<sup>2+</sup> transients, (B) caffeine-induced Ca<sup>2+</sup> transients, (C) the 50% decline in the duration (*T*<sub>50</sub>) of twitch Ca<sup>2+</sup> transients, (D) *T*<sub>50</sub> of caffeine-induced Ca<sup>2+</sup> transients, and (E) fractional SR Ca<sup>2+</sup> release obtained from cardiac myocytes isolated from wild type (WT), *mdx:utrn*<sup>-/-</sup> and *mdx:utrn*<sup>-/-</sup>:*sln*<sup>+/-</sup> mice. The total number of myocytes shown was from 3 mice per genotype. Data were analyzed by Ordinary one-way ANOVA for multigroup comparisons. ns-not statistically significant. Values shown are means ±SE.

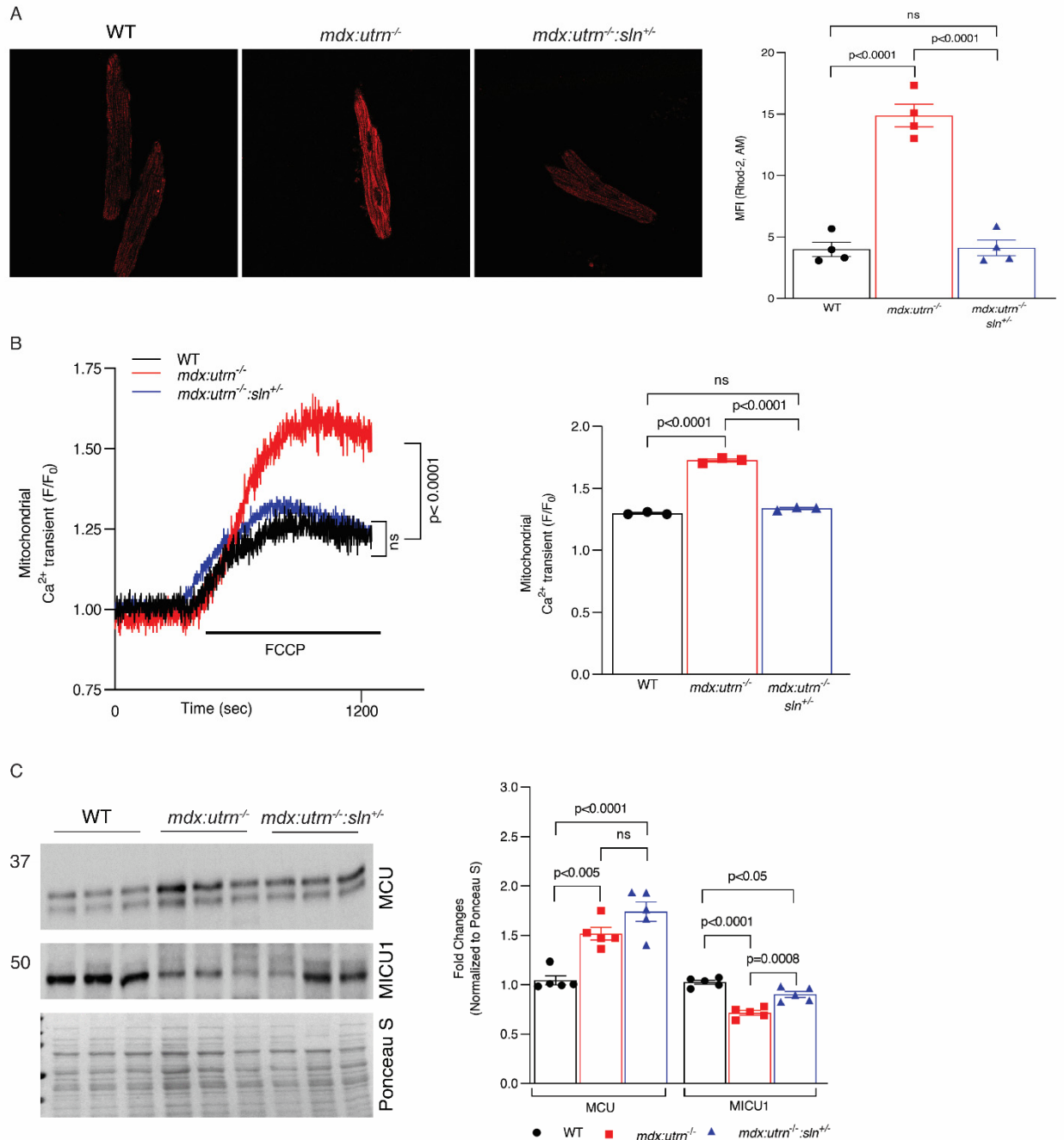


**Figure 2: Mitochondrial  $\text{Ca}^{2+}$  handling is improved in the  $\text{mdx:utrn}^{-/-}:\text{sln}^{+/-}$  myocardium. (A)** Representative confocal images of cardiac myocytes from WT,  $\text{mdx:utrn}^{-/-}$  and  $\text{mdx:utrn}^{-/-}:\text{sln}^{+/-}$  mice stained with reduced Rhod-2, AM (left panel) and summarized quantitation data showing the MFI (right panel). We used 10-25 myocytes per mouse heart.  $n=4$  mice per genotype. **(B)**

Representative traces (left panel) and quantitation of F/F<sub>0</sub> (right panel) showing mitochondrial Ca<sup>2+</sup> transients in cardiac myocytes from WT, *mdx:utrn*<sup>-/-</sup> and *mdx:utrn*<sup>-/-</sup>:*sln*<sup>+/-</sup> mice. We used 5-12 myocytes per mouse heart. n=3 mice per genotype. (C) Representative western blots (left panel) and quantitation (right panel) showing MCU and MICU1 protein levels in the ventricles of WT, *mdx:utrn*<sup>-/-</sup> and *mdx:utrn*<sup>-/-</sup>:*sln*<sup>+/-</sup> mice. For western blotting, 10 µg of protein is loaded per well. n=5 mice per genotype. Data were analyzed by Ordinary one-way ANOVA for multigroup comparisons. ns-not statistically significant. Values shown are means ±SE.

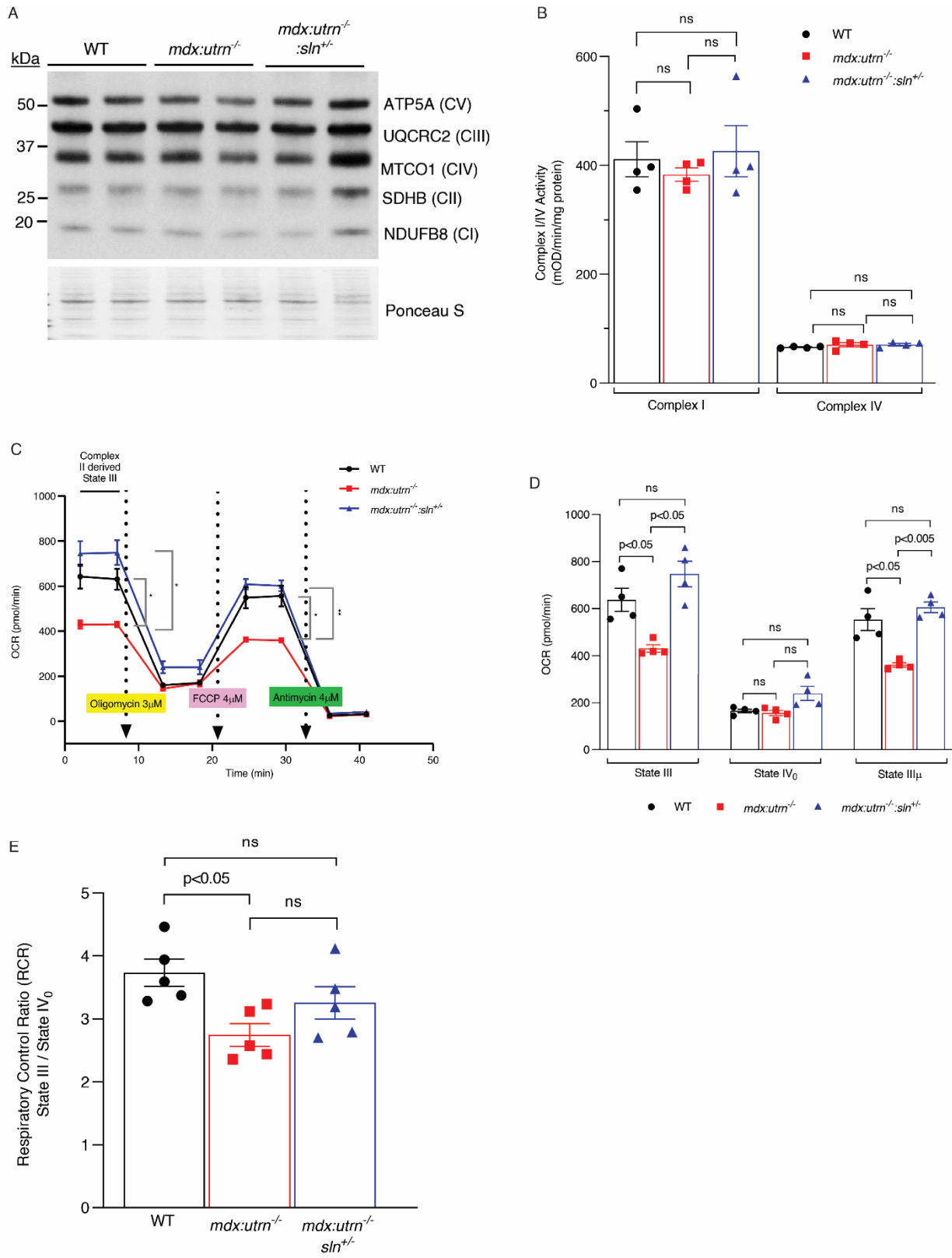


**Figure 3: Mitochondrial respiration is improved in the *mdx:utrn<sup>-/-</sup>:sln<sup>+/-</sup>* myocardium. (A)** Representative western blots showing the protein levels of electron transport chain complex I, II, III, IV, and V subunits in the ventricles of WT, *mdx:utrn<sup>-/-</sup>* and *mdx:utrn<sup>-/-</sup>:sln<sup>+/-</sup>* mice. n=4 mice per group. For western blotting, 10 µg of protein is loaded per well. **(B)** Summary of quantification showing mitochondrial complex I and complex IV activities in the ventricular lysates. n=4 mice per genotype. **(C)** Representative line graphs showing complex II driven respiration measuring oxygen consumption rate (OCR) at basal levels and after treatment with oligomycin, FCCP, and antimycin in intact heart mitochondria purified from WT, *mdx:utrn<sup>-/-</sup>* and *mdx:utrn<sup>-/-</sup>:sln<sup>+/-</sup>* mice. Quantification showing the **(D)** State III, State IV<sub>0</sub>, and State III<sub>μ</sub> respirations (n=4 mice per genotype) and **(E)** RCR (n=5 mice per genotype) in the intact heart mitochondria purified from WT, *mdx:utrn<sup>-/-</sup>* and *mdx:utrn<sup>-/-</sup>:sln<sup>+/-</sup>* mice. Sample triplicates were used for Seahorse assays. Data were analyzed by Ordinary one-way ANOVA for multigroup comparisons. ns-not statistically significant. Values shown are means ±SE.



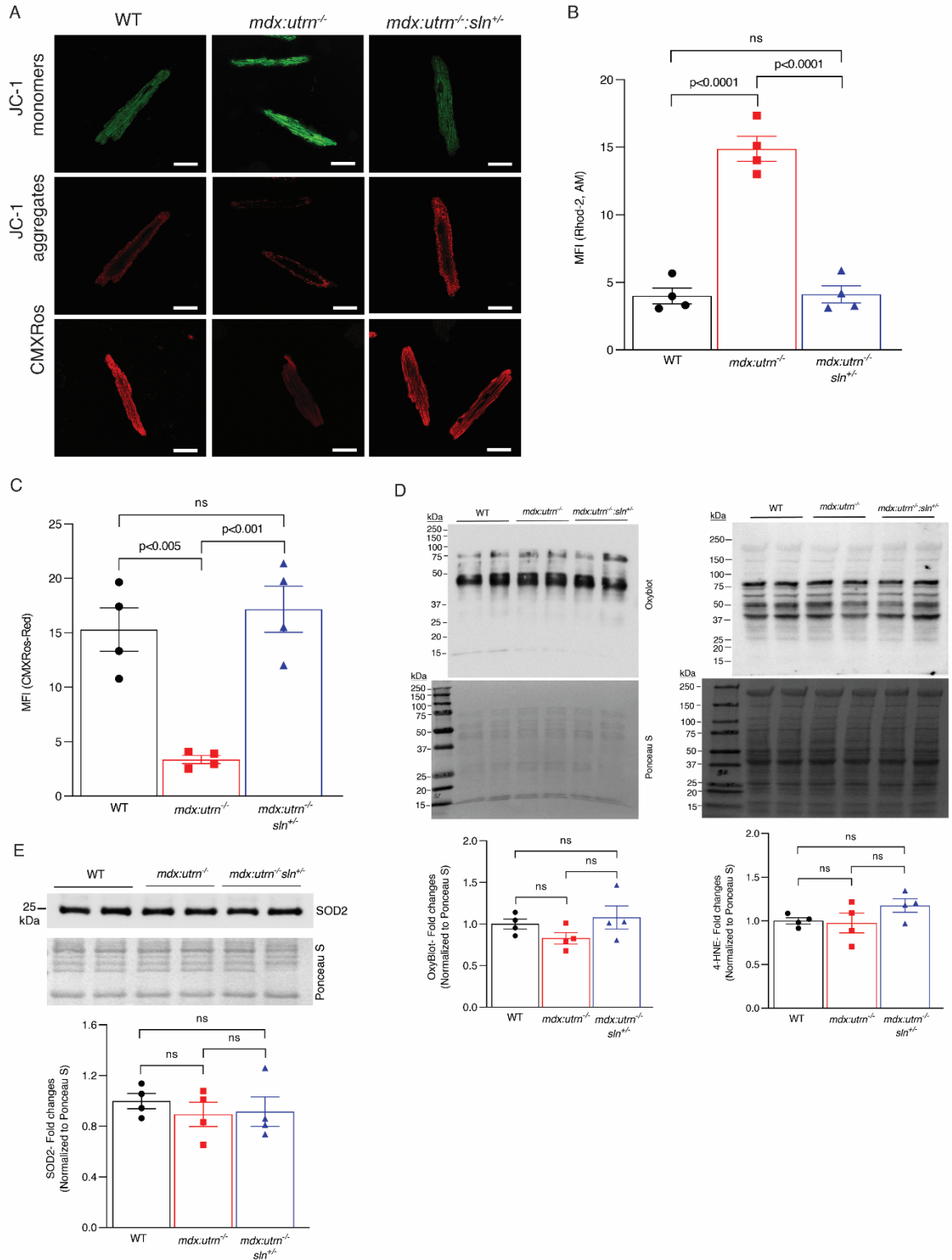


**Figure 4: Mitochondrial membrane potential is improved in the ventricular myocytes of *mdx:utrn*<sup>-/-</sup>:*sln*<sup>+/-</sup> mice. (A) Representative confocal images of ventricular myocytes stained with**

either JC-1 (15 $\mu$ M) or CMXRos (100nM). Scale bar = 25 $\mu$ m. Quantification showing the **(B)** MFI ratio of red and green of JC-1 and **(C)** MFI of CMXRos-Red as fold changes in WT, *mdx:utrn*<sup>-/-</sup> and *mdx:utrn*<sup>-/-</sup>:*sln*<sup>+/-</sup> ventricular myocytes. We used 10-25 myocytes per mouse heart. n=4 mice per genotype. **(D)** Representative OxyBlot and 4-NHE western blots (top) and quantitation (bottom) showing the levels of carbonylated proteins and lipid peroxidation in the total protein extracts prepared from the ventricles of WT, *mdx:utrn*<sup>-/-</sup> and *mdx:utrn*<sup>-/-</sup>:*sln*<sup>+/-</sup> mice. n=4 mice per genotype. **(E)** Representative western blot (top) and quantitation (bottom) showing the levels of SOD2 in the ventricles of WT, *mdx:utrn*<sup>-/-</sup> and *mdx:utrn*<sup>-/-</sup>:*sln*<sup>+/-</sup> mice. n=4 mice per genotype. For western blotting, 10  $\mu$ g of protein is loaded per well. Data were analyzed by Ordinary one-way ANOVA for multigroup comparisons. ns-not statistically significant. Values shown are means  $\pm$ SE.

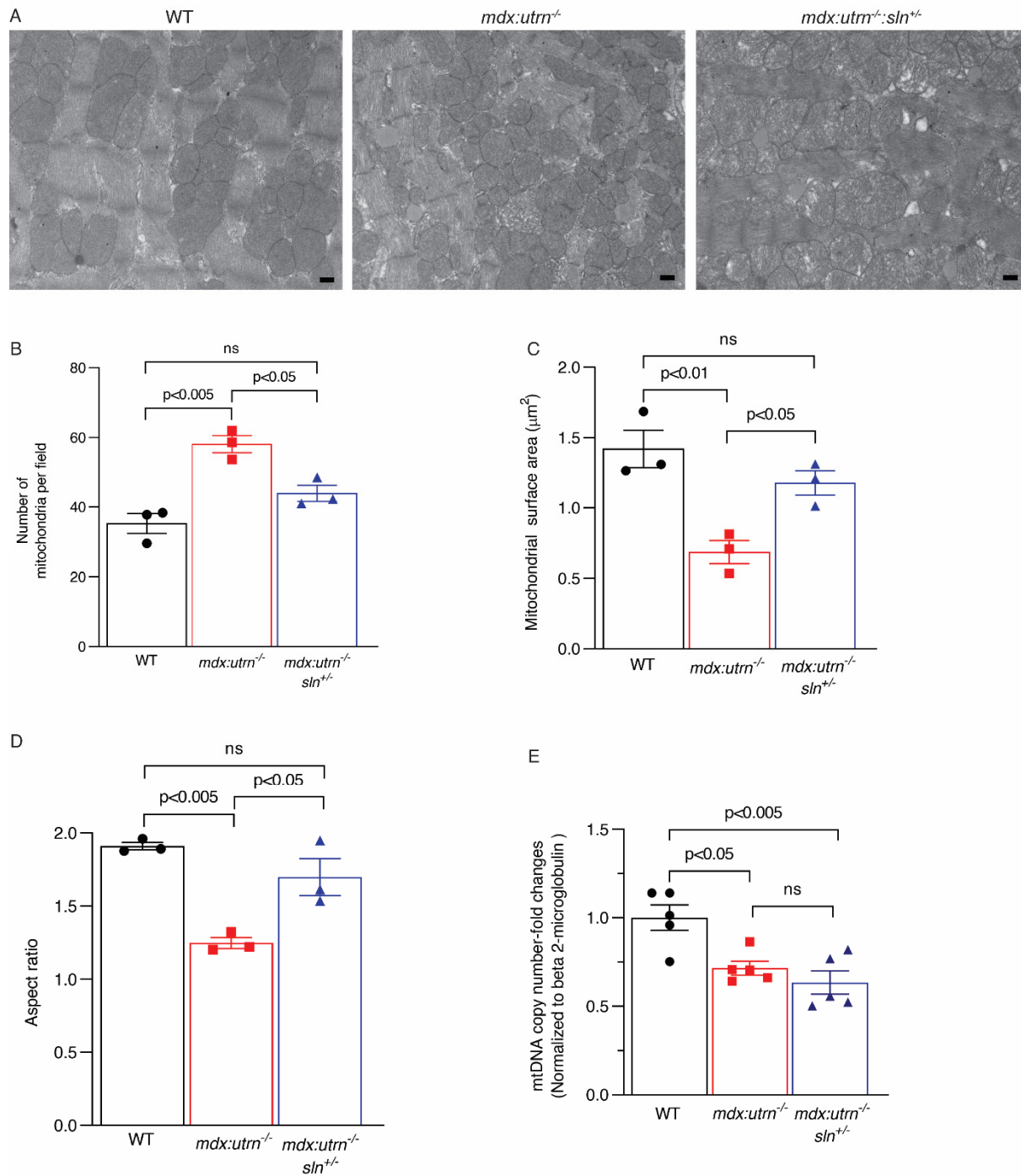


**Figure 5: Improved mitochondrial structure in *mdx:utrn*<sup>-/-</sup>:*sln*<sup>+/-</sup> ventricles.** (A) Representative transmission electron micrographs of ventricular sections from WT, *mdx:utrn*<sup>-/-</sup> and *mdx:utrn*<sup>-/-</sup>:*sln*<sup>+/-</sup> mice. Scale bar = 500 nm. Original magnification 6,300x. Quantification showing (B) mitochondrial number, (C) mitochondrial surface area (µm<sup>2</sup>), and (D) aspect ratio of mitochondria.

We randomly selected 6 to 8 fields at 6,300x and analyzed 130 to 150 mitochondria/mouse heart. n= 3 mice per genotype. **(E)** qPCR analysis showing mitochondrial copy number. n=5 mice per genotype. Data were analyzed by Ordinary one-way ANOVA for multigroup comparisons. ns-not statistically significant. Values shown are means  $\pm$ SE.

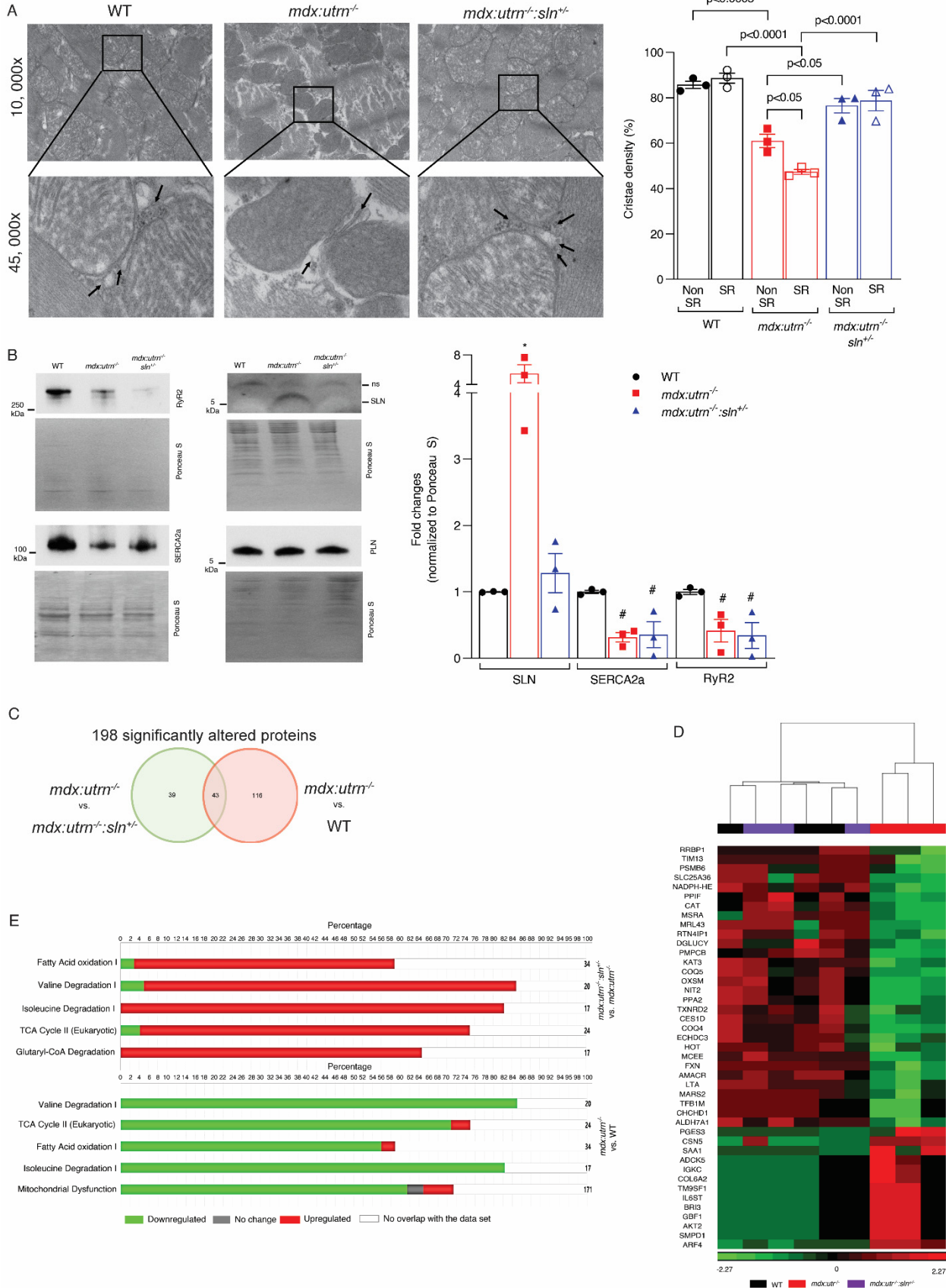


**Figure 6: Improved mitochondrial structure and MAMs in *mdx:utrn*<sup>-/-</sup>:*sln*<sup>+/-</sup> ventricles. (A)** Representative transmission electron micrographs of ventricular sections from WT, *mdx:utrn*<sup>-/-</sup> and *mdx:utrn*<sup>-/-</sup>:*sln*<sup>+/-</sup> mice (left panel). The 45,000x shows the SR-mitochondrial junctions (indicated by arrows) and loss of cristae in the SR-associated mitochondria. Quantification (right panel) showing cristae density in SR-associated and non-SR-associated mitochondria. We randomly selected 6 to 8 fields at 10,000x magnification and analyzed ~150 mitochondria/genotype (40-60 mitochondria/mouse heart) for cristae density measurements. n= 3 mice per genotype. Data were analyzed by Ordinary one-way ANOVA for multigroup comparisons. ns-not statistically significant. Values shown are means ±SE. **(B)** Representative western blots (left panel) and quantitation (right panel) showing RyR2, SERCA2a, SLN, and PLN protein levels in the MAMs purified from the myocardium of WT, *mdx:utrn*<sup>-/-</sup> and *mdx:utrn*<sup>-/-</sup>:*sln*<sup>+/-</sup> mice. 4-5 ventricles were pooled for each MAMs preparation. n=3 MAMs preparation/per genotype. For western blotting, 10-20 µg of MAMs protein is loaded per well. Data were analyzed by Ordinary one-way ANOVA for multigroup comparisons. ns-not statistically significant. Values shown are means ±SE. **(C)** Venn diagram showing significantly altered MAMs proteins between *mdx:utrn*<sup>-/-</sup>& WT and *mdx:utrn*<sup>-/-</sup>:*sln*<sup>+/-</sup> & *mdx:utrn*<sup>-/-</sup> mice. **(D)** Heat map of 43 MAMs proteins that are well clustered between WT and *mdx:utrn*<sup>-/-</sup>:*sln*<sup>+/-</sup> but differentially expressed in *mdx:utrn*<sup>-/-</sup> mice. **(E)** Horizontal stacked bar chart comparing the top canonical pathways either up-or down-regulated in the MAMs between *mdx:utrn*<sup>-/-</sup>:*sln*<sup>+/-</sup> and *mdx:utrn*<sup>-/-</sup> and between *mdx:utrn*<sup>-/-</sup> & WT mice with a p-value of 0.05 cutoff.